LETTER

doi:10.1038/nature13729

Experimental realization of universal geometric quantum gates with solid-state spins

C. Zu[1], W.-B. Wang[1], L. He[1], W.-G. Zhang[1], C.-Y. Dai[1], F. Wang[1] & L.-M. Duan[1,2]

Experimental realization of a universal set of quantum logic gates is the central requirement for the implementation of a quantum computer. In an 'all-geometric' approach to quantum computation[1,2], the quantum gates are implemented using Berry phases[3] and their non-Abelian extensions, holonomies[4], from geometric transformation of quantum states in the Hilbert space[5]. Apart from its fundamental interest and rich mathematical structure, the geometric approach has some built-in noise-resilience features[1,2,6,7]. On the experimental side, geometric phases and holonomies have been observed in thermal ensembles of liquid molecules using nuclear magnetic resonance[8,9]; however, such systems are known to be non-scalable for the purposes of quantum computing[10]. There are proposals to implement geometric quantum computation in scalable experimental platforms such as trapped ions[11], superconducting quantum bits[12] and quantum dots[13], and a recent experiment has realized geometric single-bit gates in a superconducting system[14]. Here we report the experimental realization of a universal set of geometric quantum gates using the solid-state spins of diamond nitrogen–vacancy centres. These diamond defects provide a scalable experimental platform[15–17] with the potential for room-temperature quantum computing[16–19], which has attracted strong interest in recent years[20]. Our experiment shows that all-geometric and potentially robust quantum computation can be realized with solid-state spin quantum bits, making use of recent advances in the coherent control of this system[15–20].

Under adiabatic cyclic evolution, a non-degenerate eigenstate of a quantum system acquires a phase factor, which has a dynamical component proportional to the time integral of the eigenstate energy and a geometric component determined by the global property of the evolution path. This geometric phase, first discovered by Berry[3], has been linked with many important physics phenomena[21]. If the system has degenerate eigenstates, the Berry phase is replaced by a geometric unitary operator acting on the degenerate subspace, called a holonomy by analogy with differential geometry. The holonomies do not in general commute with each other. In the proposed geometric approach to quantum computation[1,2], such holonomies are exploited to realize a universal set of quantum gates, compositions of which then can be used to perform arbitrary quantum computation tasks. Because holonomies are determined by global geometric properties, geometric computation is more robust to certain control errors[1,2,6,7]. The implementation of geometric quantum computation has been proposed in several quantum bit (qubit) systems[11–13]; however, it remains experimentally challenging to realize a universal set of gates using holonomies alone, because of the requirements of slow adiabatic evolution and a complicated level structure.

In the recent proposal of non-adiabatic geometric quantum computation[6,22], universal quantum gates are constructed fully by geometric means without the requirement of adiabatic evolution, thereby combining speed with universality. Under a cyclic evolution of the system Hamiltonian $H(t)$ (with $H(\tau) = H(0)$, where τ is the cycle period), we let $|\xi_l(t)\rangle$ ($l = 1, 2, \ldots, M$) denote instantaneous orthonormal bases (moving frames) which coincide with the basis vectors $|\xi_l\rangle$ of the computational space C at $t = 0$ and $t = \tau$, with $|\xi_l(\tau)\rangle = |\xi_l(0)\rangle = |\xi_l\rangle$. The evolution operator $U(\tau)$ for the basis states $|\xi_l\rangle$ has two contributions: a dynamic part and a fully geometric part[6]. If the parallel-transport condition $\langle\xi_l(t)|H(t)|\xi_{l'}(t)\rangle = 0$ is satisfied for any l and l' at any time t, then the dynamic contribution becomes identically zero and $U(\tau)$ is given by

$$U(\tau) = T\exp\left[i\int_0^\tau A\,\mathrm{d}t\right] \quad (1)$$

where T indicates time-ordered integration and $A = [A_{ll'}] = [\langle\xi_l(t)|i\partial_t|\xi_{l'}(t)\rangle]$ is the $M \times M$ connection matrix[6]. The form of $U(\tau)$ is identical to the Wilczek–Zee holonomy in the adiabatic case[4,6].

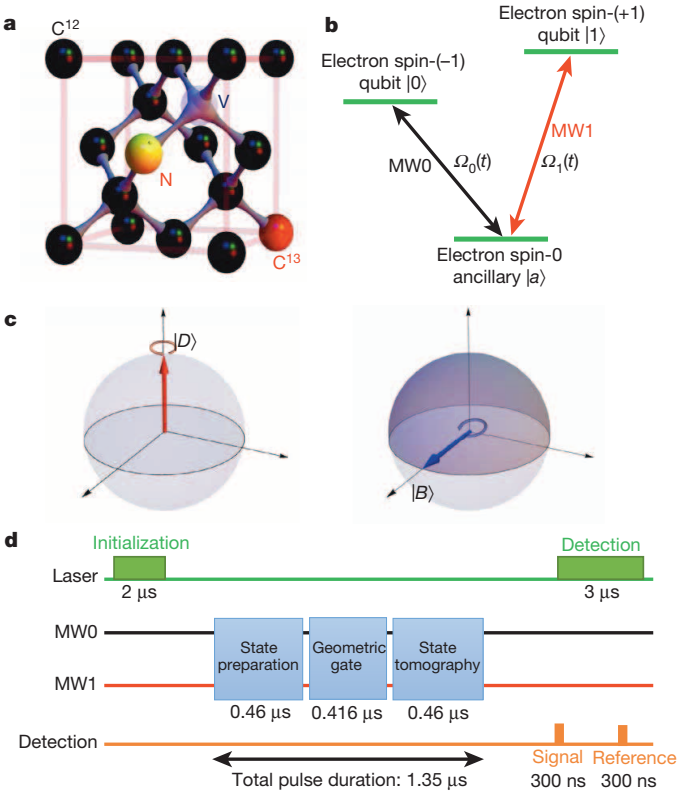

Figure 1 | Geometric gates in a diamond nitrogen–vacancy centre. **a**, Illustration of a nitrogen–vacancy (NV) centre in a diamond with a proximal C^{13} atom. **b**, Encoding of a qubit in the spin-triplet ground state of the nitrogen–vacancy centre and the microwave coupling configuration. The spin-0 state provides an ancillary level $|a\rangle$ for geometric manipulation of the qubit. **c**, A geometric picture of the holonomic gates. Under a cyclic Hamiltonian evolution, the dark state $|D\rangle$ and the bright state $|B\rangle$ rotate by 2π around the North Pole of the Bloch sphere and, respectively, along its equator, acquiring geometric phase of 0 and, respectively, π (half of the swept solid angle). When we choose different forms of the dark and bright states, by controlling parameters in the Hamiltonian, this state-dependent geometric phase leads to the corresponding holonomic gates. **d**, The time sequence for implementation and verification of single-qubit geometric gates.

[1]Center for Quantum Information, IIIS, Tsinghua University, Beijing 100084, China. [2]Department of Physics, University of Michigan, Ann Arbor, Michigan 48109, USA.

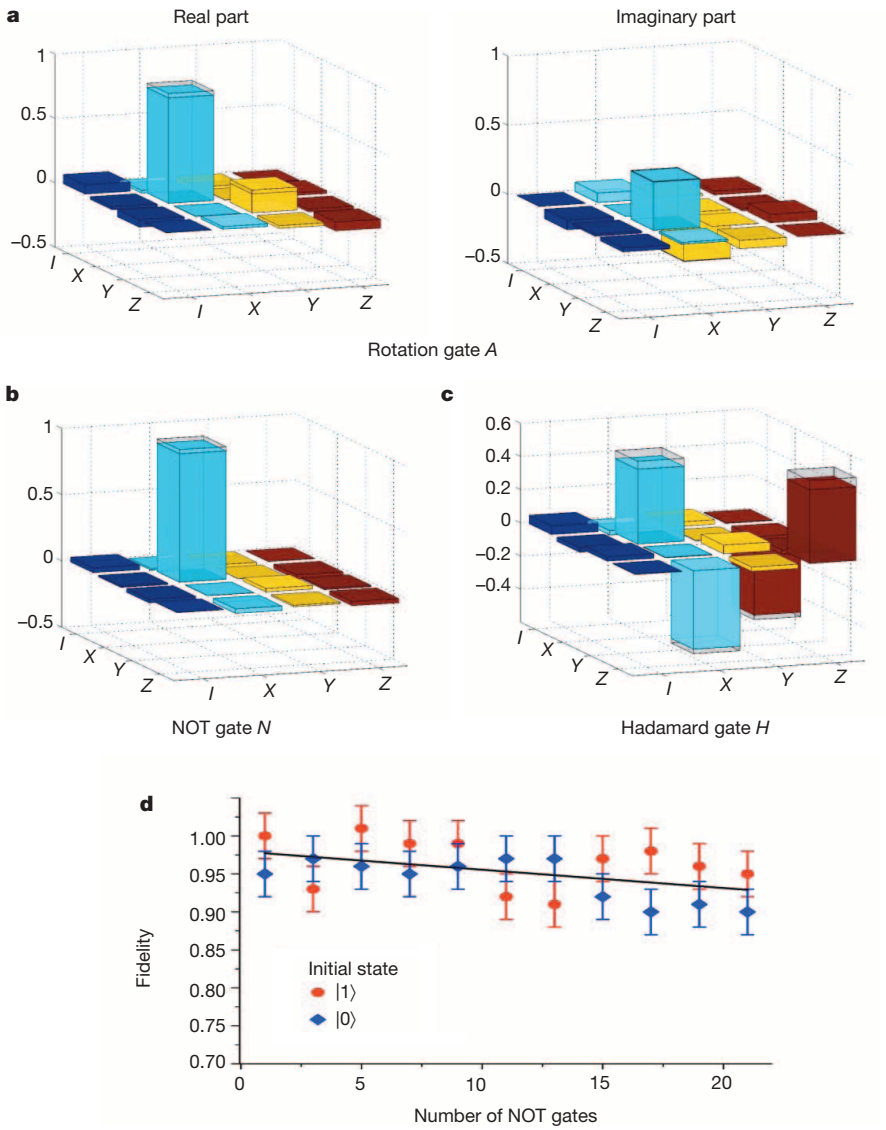

Figure 2 | Experimental results for single-bit geometric gates. **a**–**c**, The measured process matrix elements for the rotation gate A (**a**), the NOT gate N (**b**) and the Hadamard gate H (**c**). The measured tiny imaginary parts of the process matrices for the NOT and Hadamard gates are not shown. The hollow caps in these figures denote the corresponding matrix elements for the ideal gates. **d**, The measured fidelities of the final states compared with the ideal output (error bars denote s.d.) after application of a sequence of the geometric NOT gates to initial states $|0\rangle$ and $|1\rangle$. By fitting the data under the assumption of independent error for each gate, we obtain the error induced by each NOT gate at $(0.24 \pm 0.06)\%$.

Our experiment realizes a universal set of quantum gates using only non-adiabatic holonomies[6]. Single-bit gates, together with entangling controlled-NOT (CNOT) operation, are universal for quantum computation. Our realization is based on the control of electron and nuclear spins in a diamond nitrogen–vacancy centre that effectively form a quantum register[20]. To realize the single-bit geometric gates, we manipulate the electron spin states of a nitrogen–vacancy centre (Fig. 1a) in a synthetic diamond at room temperature (see Methods for a description of the experimental set-up). The nitrogen–vacancy centre has a spin-triplet ground state. We take the Zeeman components $|m=-1\rangle \equiv |0\rangle$ and $|m=+1\rangle \equiv |1\rangle$ as the qubit basis states and use $|m=0\rangle \equiv |a\rangle$ as an ancillary level for geometric manipulation of the qubit. The spin state is initialized through optical pumping to the $|m=0\rangle$ level and read out by distinguishing different fluorescence levels of the states under illumination of a short green laser pulse[20] (see Methods for the calibration of fluorescence levels of different states). We apply a magnetic field of 451 G along the nitrogen–vacancy axis using a permanent magnet. Under this field, the nearby nuclear spins are polarized by optical pumping[23], enhancing the coherence time of the electron spin.

The transitions from the qubit states $|0\rangle$ and $|1\rangle$ to the ancillary level $|a\rangle$ are coupled by microwave pulses controlled using an arbitrary-waveform generator, with Rabi frequencies $\Omega_0(t)$ (for the $|0\rangle \rightarrow |a\rangle$ transition) and $\Omega_1(t)$ (for the $|1\rangle \rightarrow |a\rangle$ transition) (Fig. 1b). We vary the amplitude $\Omega(t)=\sqrt{\Omega_0^2+\Omega_1^2}$ but fix the ratio $\Omega_1/\Omega_0 = e^{i\varphi}\tan(\theta)$ to be constant. The Hamiltonian for the coupling between these three levels takes the form

$$H_1(t) = \hbar\Omega(t)\left[\left(\cos(\theta)|0\rangle + e^{i\phi}\sin(\theta)|1\rangle\right)\langle a| + \text{H.c.}\right]$$

where $\hbar$ is Planck's constant divided by 2π and H.c. denotes the Hermitian conjugate. We define the bright state as $|B\rangle = \cos(\theta)|0\rangle + e^{i\varphi}\sin(\theta)|1\rangle$ and the dark state as $|D\rangle = -e^{-i\varphi}\sin(\theta)|0\rangle + \cos(\theta)|1\rangle$. When $\Omega(t)$ makes a cyclic evolution with $\Omega(0)=\Omega(\tau)=0$, the bright state evolves as $|B(t)\rangle = e^{i\alpha(t)}[\cos(\alpha(t))|B\rangle + \sin(\alpha(t))|a\rangle]$, where $\alpha(t) \equiv \int_0^t \Omega(t')\,dt'$, while the dark state remains unchanged. After a cyclic evolution with $\alpha(\tau)=\pi$, the bright and dark states pick up geometric phases of π and 0, respectively (Fig. 1c). We take the moving frame as $|\xi_0(t)\rangle = \cos(\theta)|B(t)\rangle - e^{i\varphi}\sin(\theta)|D\rangle$, $|\xi_1(t)\rangle = e^{-i\varphi}\sin(\theta)|B(t)\rangle + \cos(\theta)|D\rangle$, which makes a cyclic evolution with $|\xi_l(0)\rangle = |\xi_l(\tau)\rangle = |l\rangle$ $(l=0,1)$. For this evolution, it can easily be checked that the condition $\langle\xi_l(t)|H(t)|\xi_{l'}(t)\rangle = 0$ is always satisfied, such that there is no dynamic contribution to the evolution operator $U(\tau)$ (ref. 6). Using equation (1), we find the holonomy

$$U(\tau) = \begin{bmatrix} -\cos(2\theta) & -e^{i\varphi}\sin(2\theta) \\ -e^{-i\varphi}\sin(2\theta) & \cos(2\theta) \end{bmatrix}$$

in the computational basis $\{|0\rangle, |1\rangle\}$.

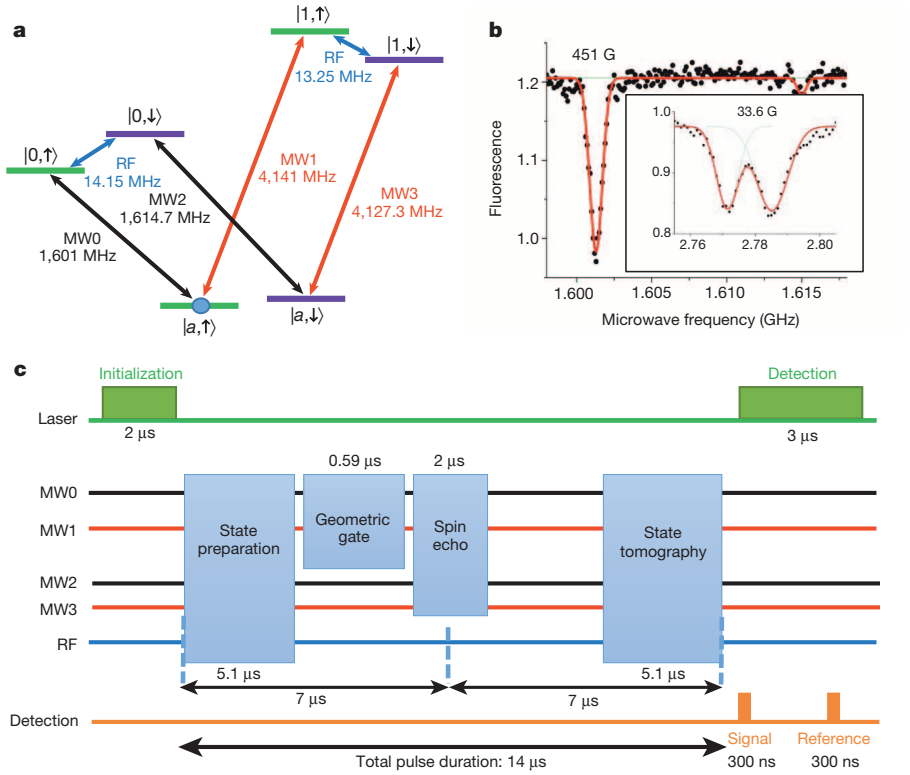

Figure 3 | Level scheme and pulse sequence for the geometric CNOT gate. **a**, The level structure of the electron and the nuclear spins for the geometric CNOT gate and the microwave and radio-frequency (RF) coupling configuration. **b**, Optically detected magnetic resonance spectroscopy obtained by measuring the fluorescence level while scanning the frequency of the microwave that couples to the transition between $|a\rangle$ (spin 0) and $|1\rangle$ (spin 1). The two dips at 33.6 G (inset) represent the hyperfine splitting caused by the unpolarized nuclear spin. The very asymmetric dips at 451 G indicate that the nuclear spin has been polarized. **c**, The time sequence for implementation and verification of the geometric CNOT gate between the electron and the nuclear spins. The CNOT gate is implemented by applying the pulses MW0 and MW1 simultaneously. Microwave pulses MW2 and MW3 are used, in addition to MW0 and MW1, to implement a spin echo to increase the spin coherence time. To verify the CNOT gate, we use a combination of MW0–MW3 and a radio-frequency pulse to prepare various initial superposition states and measure the final output in different bases through quantum state tomography.

We evolve the Rabi frequencies $\Omega_i(t)$ along three different loops, with the parameters (θ, φ) chosen respectively as $(3\pi/4, 0)$, $(3\pi/4, \pi/8)$ and $(5\pi/8, 0)$. The three geometric gates resulting from these cyclic evolutions are denoted by the NOT gate N, the rotation gate A and the Hadamard gate H, respectively. The combination of gates N and A gives the well-known $\pi/8$-gate $T = NA$. Together, N, A and H make a universal set of single-bit gates. To characterize these geometric gates, we use quantum process tomography by preparing and measuring the qubit in different bases[24], with the time sequence shown in Fig. 1d. The matrix elements for each process are shown in Fig. 2a–c, which are shown, for comparison, with the corresponding elements of the ideal gates. From the process tomography (Methods), we find the process fidelities $F_P = (96.5 \pm 1.9)\%$, $(96.9 \pm 1.5)\%$ and $(92.1 \pm 1.8)\%$ for the N, A and H gates, respectively. The major contribution to the infidelity actually comes from the state preparation and detection error in the quantum process tomography. To measure the intrinsic gate error, we concatenate a series of

a

Two-qubit geometric CNOT gate						
Initial state	$\|0,\uparrow\rangle$	$\|0,\downarrow\rangle$	$\|1,\uparrow\rangle$	$\|1,\downarrow\rangle$	$\|0\rangle(\|\uparrow\rangle + \|\uparrow\rangle)$	$\|0\rangle(\|\uparrow\rangle + i\|\downarrow\rangle)$
Ideal final state	$\|1,\uparrow\rangle$	$\|0,\downarrow\rangle$	$\|0,\uparrow\rangle$	$\|1,\downarrow\rangle$	$\|1,\uparrow\rangle + \|0,\downarrow\rangle$	$\|1,\uparrow\rangle + i\|0,\downarrow\rangle$
Measured fidelity	0.99(1)	0.97(1)	0.87(1)	0.94(2)	0.90(3)	0.86(4)

b

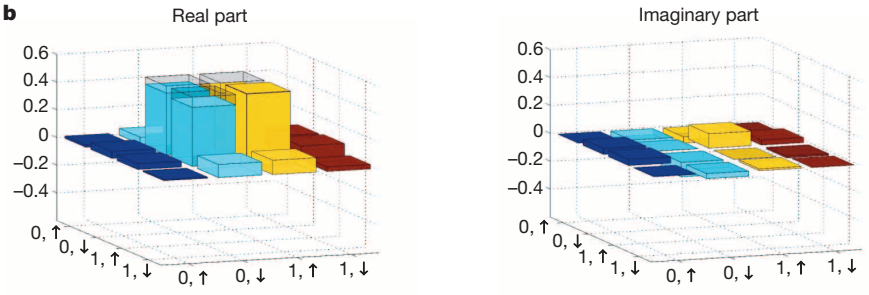

Figure 4 | Experimental results for the geometric CNOT gate. **a**, Measured output state fidelities of the geometric CNOT gate under a few typical input states, where the number in the bracket represents the error bar (s.d.) in the last digit. **b**, The matrix elements of the output density operator reconstructed through quantum state tomography when the geometric CNOT is applied to the product state $|0\rangle(|\uparrow\rangle + |\downarrow\rangle)/\sqrt{2}$. The hollow caps denote the matrix elements for the ideal output state under a perfect gate.

gates and examine the fidelity decay as the number of gates increases[19]. As an example, we show in Fig. 2d the fidelity decay by concatenating the NOT gates. From the data, we find that the intrinsic error per gate is about 0.24%. This can be compared with the 1% error rate for the dynamic NOT gate using optimized pulses and the same method of measurement[19]. The achieved high fidelity indicates that geometric manipulation is indeed resilient to control errors.

To realize the geometric quantum CNOT gate, we use one nearby C^{13} nuclear spin as the control qubit (with the basis vectors $|\uparrow\rangle$ and $\langle\downarrow|$) and the nitrogen–vacancy centre electron spin as the target qubit[25]. Both the electron spin and the nuclear spin are polarized through optical pumping under the 451 G magnetic field, which is confirmed by optically detected magnetic resonance spectroscopy (Fig. 3b). The spins are interacting with each other through hyperfine and dipole couplings, and the resultant level configuration is shown in Fig. 3a. By applying state-selective microwave and radio-frequency pulses, we can couple different levels. In particular, for the microwave pulses MW0 and MW1, with respective Rabi frequencies $\Omega_0(t)$ and $\Omega_1(t)$, we have the following coupling Hamiltonian:

$$H_2(t) = \hbar\Omega(t)[(|0,\uparrow\rangle - |1,\uparrow\rangle)\ \langle a,\uparrow| + \text{H.c.}]/\sqrt{2}$$

Here we have fixed the ratio $\Omega_1/\Omega_0 = -1$. Under cyclic evolution of $\Omega(t)$ with $\int_0^\tau \Omega(t)\ \mathrm{d}t = \pi$, we find the holonomy $U(\tau) = |\uparrow\rangle\langle\uparrow| \otimes N + |\downarrow\rangle\langle\downarrow| \otimes I$ using equation (1), where I denotes the 2×2 unit matrix. This achieves the quantum CNOT gate exactly.

To characterize the geometric CNOT gate, we apply the gate to the qubit basis states as well as their superpositions, and measure the fidelity of the final states relative to the ideal outputs, by quantum state tomography[24]. The superposition of the nuclear spin states required for state preparation and measurement is generated using radio-frequency pulses, which takes longer than it would with microwave pulses owing to the much smaller magnetic moment of the nuclear spin. The electron spin decoherence is significant during the slow radio-frequency pulses. To correct that, we apply a Hahn spin echo in the middle of the whole operation with the time sequence shown in Fig. 3c. The measured state fidelities are listed in Fig. 4a under typical input states. A hallmark of the entangling operation is that the geometric CNOT gate generates entanglement from the initial product state. As an example, for the input state $|0\rangle \otimes (|\uparrow\rangle + |\downarrow\rangle)$ (unnormalized), the matrix elements of the output density operator are shown in Fig. 4b, with a measured entanglement fidelity of $(90.2 \pm 2.5)\%$ and a concurrence of 0.85 ± 0.05, which unambiguously confirms entanglement[10].

Our experimental realization of a universal set of holonomic gates using individual spins paves the way for all-geometric quantum computation in a solid-state system. The electron and nuclear spins of different nitrogen–vacancy centres can be wired up quantum mechanically to form a scalable network of qubits through, for example, direct dipole interaction[16,18], spin-chain assisted coupling by the nitrogen dopants[17,26] or photon-mediated coupling[15,27,28]. The technique used here for the geometric realization of universal gates may also find applications in other scalable experimental systems, such as trapped ions or superconducting qubits. The geometric phase is closely related to the topological phase[29,30], and the demonstration of gates using only holonomies is a step towards realization of topological computation[30], the most robust way of quantum computing.

Online Content Methods, along with any additional Extended Data display items and Source Data, are available in the online version of the paper; references unique to these sections appear only in the online paper.

Received 6 May; accepted 31 July 2014.

1. Zanardi, P. & Rasetti, M. Holonomic quantum computation. *Phys. Lett. A* **264,** 94–99 (1999).
2. Pachos, J., Zanardi, P. & Rasetti, M. Non-Abelian Berry connections for quantum computation. *Phys. Rev. A* **61,** 010305(R) (2000).
3. Berry, M. V. Quantal phase-factors accompanying adiabatic changes. *Proc. R. Soc. Lond. A* **392,** 45–57 (1984).
4. Wilczek, F. & Zee, A. Appearance of gauge structure in simple dynamical systems. *Phys. Rev. Lett.* **52,** 2111–2114 (1984).
5. Lloyd, S. Computation from geometry. *Science* **292,** 1669 (2001).
6. Sjöqvist, E. *et al.* Non-adiabatic holonomic quantum computation. *New J. Phys.* **14,** 103035 (2012).
7. Johansson, M. *et al.* Robustness of non-adiabatic holonomic gates. *Phys. Rev. A* **86,** 062322 (2012).
8. Jones, J. A., Vedral, V., Ekert, A. & Castagnoli, G. Geometric quantum computation using nuclear magnetic resonance. *Nature* **403,** 869–871 (2000).
9. Feng, G., Xu, G. & Long, G. Experimental realization of nonadiabatic holonomic quantum computation. *Phys. Rev. Lett.* **110,** 190501 (2013).
10. Nielsen, M. A. & Chuang, I. L. *Quantum Computation and Quantum Information* (Cambridge Univ. Press, 2010).
11. Duan, L. M., Cirac, J. I. & Zoller, P. Geometric manipulation of trapped ions for quantum computation. *Science* **292,** 1695–1697 (2001).
12. Falci, G. *et al.* Detection of geometric phases in superconducting nanocircuits. *Nature* **407,** 355–358 (2000).
13. Solinas, P., Zanardi, P., Zanghi, N. & Rossi, F. Holonomic quantum gates: a semiconductor-based implementation. *Phys. Rev. A* **67,** 062315 (2003).
14. Abdumalikov, A. A. *et al.* Experimental realization of non-Abelian non-adiabatic geometric gates. *Nature* **496,** 482–485 (2013).
15. Pfaff, W. *et al.* Unconditional quantum teleportation between distant solid-state quantum bits. *Science* **345,** 532–535 (2014).
16. Neumann, P. *et al.* Scalable quantum register based on coupled electron spins in a room temperature solid. *Nature Phys.* **6,** 249–253 (2010).
17. Yao, N. Y. *et al.* Scalable architecture for a room temperature solid-state quantum information processor. *Nature Commun.* **3,** 800 (2012).
18. Dolde, F. *et al.* Room-temperature entanglement between single defect spins in diamond. *Nature Phys.* **9,** 139–143 (2013).
19. Dolde, F. *et al.* High-fidelity spin entanglement using optimal control. *Nature Commun.* **5,** 3371 (2014).
20. Doherty, M. W. *et al.* The nitrogen-vacancy colour centre in diamond. *Phys. Rep.* **528,** 1–45 (2013).
21. Shapere, A. & Wilczek, F. *Geometric Phases in Physics* (World Scientific, 1989).
22. Zhu, S. L. & Wang, Z. D. Implementation of universal quantum gates based on nonadiabatic geometric phases. *Phys. Rev. Lett.* **89,** 097902 (2002).
23. Jacques, V. *et al.* Dynamic polarization of single nuclear spins by optical pumping of nitrogen-vacancy color centers in diamond at room temperature. *Phys. Rev. Lett.* **102,** 057403 (2009).
24. White, A. G. *et al.* Measuring two-qubit gates. *J. Opt. Soc. Am. B* **24,** 172–183 (2007).
25. Jelezko, F. *et al.* Observation of coherent oscillation of a single nuclear spin and realization of a two-qubit conditional quantum gate. *Phys. Rev. Lett.* **93,** 130501 (2004).
26. Yao, N. Y. *et al.* Robust quantum state transfer in random unpolarized spin chains. *Phys. Rev. Lett.* **106,** 040505 (2011).
27. Jiang, L., Taylor, J. M., Sorensen, A. S. & Lukin, M. D. Distributed quantum computation based-on small quantum registers. *Phys. Rev. A* **76,** 062323 (2007).
28. Duan, L. M. & Monroe, C. Quantum networks with trapped ions. *Rev. Mod. Phys.* **82,** 1209 (2010).
29. Loredo, J. C., Broome, M. A., Smith, D. H. & White, A. G. Observation of entanglement-dependent two-particle holonomic phase. *Phys. Rev. Lett.* **112,** 143603 (2014).
30. Pachos, J. K. *Introduction to Topological Quantum Computation* (Cambridge Univ. Press, 2012).

Acknowledgements We thank M. Lukin's group for discussions. This work was supported by the National Basic Research Program of China 2011CBA00302 and the quantum information project from the Ministry of Education of China. In addition, L.-M.D. acknowledges support from the IARPA MUSIQC program, the AFOSR and the ARO MURI program.

Author Contributions L.-M.D. had the idea for the experiment and supervised the project. C.Z., W.-B.W., L.H., W.-G.Z., C.-Y.D., F.W. carried out the experiment. L.-M.D. and C.Z. wrote the manuscript.

Author Information Reprints and permissions information is available at www.nature.com/reprints. The authors declare no competing financial interests. Readers are welcome to comment on the online version of the paper. Correspondence and requests for materials should be addressed to L.-M.D. (lmduan@umich.edu).

METHODS

Experimental set-up. We use a home-built confocal microscopy, with an oil-immersed objective lens (NA = 1.49), to address and detect single nitrogen–vacancy centres in a type-IIa, single-crystal synthetic diamond sample (Element Six). A 532 nm diode laser, controlled by an acoustic optical modulator (AOM), is used for spin-state initialization and detection. We collect fluorescence photons (wavelength ranging from 637 to 850 nm) into a single-mode fibre and detect them using the single-photon counting module (SPCM), with a counting rate of 105 kHz and a signal-to-noise ratio of 15:1. The diamond sample is mounted on a three-axis, closed-loop piezoelectric actuator for submicrometre-resolution scanning. An impedance-matched gold coplanar waveguide (CPW) with a 70 μm gap, deposited on a coverslip, is used for delivery of radio-frequency and microwave signals to the nitrogen–vacancy centre.

In our experiment, we find a single nitrogen–vacancy centre with a proximal C^{13} of 13.7 MHz hyperfine strength (Fig. 1). To polarize the nearby nuclear spins (C^{13} and the host N^{14}), we apply a magnetic field of 451 G along the nitrogen–vacancy axis using a permanent magnet. Under this field, the electron spin levels $|m=0\rangle$ and $|m=-1\rangle$ become almost degenerate in the optically excited state (called the esLAC, the electron-spin level anti-crossing[23]), which facilitates electron-spin/nuclear-spin flip-flop process during optical pumping. The spin flip-flop process leads to polarization of the nitrogen nuclear spin on the nitrogen–vacancy site and the nearby C^{13} nuclear spins after 2 μs green laser illumination[23]. The Zeeman energy from the 451 G magnetic field shifts the respective energy differences between electron spin states $|m=0\rangle$ and $|-1\rangle$ and $|0\rangle$ and $|+1\rangle$ from the zero-field splitting, 2,870 MHz, to 1,601 MHz and 4,141 MHz, and shifts the corresponding nuclear-spin hyperfine splittings for the $|-1\rangle$ and $|+1\rangle$ levels from 13.7 MHz to 14.15 MHz and 13.25 MHz. Owing to the large energy difference of the $m=\pm1$ levels, we apply two independent microwave sources (Rohde–Schwarz), locked by a 10 MHz reference rubidium clock, to address each transition. To adjust the frequency and phase of the microwave pulses, we mix each microwave output with an arbitrary-waveform generator (AWG; Tektronix; 500 MHz sample rate). Radio-frequency signals for nuclear spin manipulation are generated directly by another analogue channel of the AWG. All the microwave and radio-frequency signals are amplified by independent amplifiers, combined through a home-made circuit, and delivered to the CPW. The digital markers of the AWG are used to control the pulse sequence (including the laser and the SPCM) with a timing resolution of 2 ns.

For each experimental cycle, we start the sequence with 2 μs of laser illumination to polarize the nitrogen–vacancy electron spin and nearby nuclear spins, and end it with a 3 μs laser pulse for spin state detection. We collect signal photons for 300 ns right after the detection laser rises (reaches full intensity), and for another 300 ns for reference 2 μs later. With a photon collection rate of 105 kHz, we have an average of 0.03 photon counts per cycle. To measure each datum, we repeat the experimental cycle at least 10^6 times, resulting in a total photon count of 3×10^4. The error bars of our data account for the statistical error associated with the photon counting. To calculate the error bar of each datum, we use Monte Carlo simulation by assuming a Poissonian distribution for the photon counts. For each simulation trial, we calculate the value of each datum. Then, by sampling over all the trails according to the Poissonian distribution, we get the statistics of the data (including their mean value and standard deviation (the error bar)).

Calibration of fluorescence levels for different states. Owing to the esLAC that induces spin flip-flop during the detection and the imperfect initial polarization of the electron and nuclear spins, each spin component $|m,m_n\rangle$ ($m=0,\pm1$; $m_n=\uparrow,\downarrow$) may fluorescence at different levels. We note that the spins are predominantly in the state $|m=0,m_n=\uparrow\rangle$ after the optical pumping. To calibrate the fluorescence level of each state, we therefore associate the detected fluorescence level right after the optical pumping with the state $|m=0,\ m_n=\uparrow\rangle$. With microwave or radio-frequency π-pulses (the π-pulses are calibrated through Rabi oscillations), we can make a complete transfer between $|m=0,m_n=\uparrow\rangle$ and any other $|m,m_n\rangle$ spin component. For instance, with a π-pulse between $|m=0,m_n=\uparrow\rangle$ and $|m=0,m_n=\downarrow\rangle$ right after the optical pumping, we associate the detected fluorescence level with the $|m=0,\ m_n=\downarrow\rangle$ state. In this way, the characteristic fluorescence level of each component $|m,m_n\rangle$ can be calibrated. With the calibrated fluorescence level for each spin component, we then read out the system state after the geometric gates through quantum state tomography[24].

Quantum process tomography. A quantum process can be described by a completely positive map ε acting on an arbitrary initial state ρ_i, transferring it to $\rho_f\equiv\varepsilon(\rho_i)$. In quantum process tomography (QPT), we choose a fixed set of basis operators $\{E_m\}$ so that the map $\varepsilon(\rho_i)=\sum_{mn}E_m\rho_iE_n^\dagger\chi_{mn}$ is identified with a process matrix χ_{mn}. We experimentally measure this process matrix χ by the maximum-likelihood technique[24]. For single-bit QPT, we set the basis operators to be $I=I, X=\sigma_x, Y=-i\sigma_y, Z=\sigma_z$ and choose the four different initial states $|0\rangle$, $|1\rangle$, $(|0\rangle+|1\rangle)/\sqrt{2}$ and $(|0\rangle-i|1\rangle)/\sqrt{2}$. We reconstruct the corresponding final density operators through the standard quantum state tomography and use them to calculate the process matrix χ_e. This process matrix χ_e is compared with the ideal one χ_{id} by calculating the process fidelity $F_P=\mathrm{Tr}(\chi_e\chi_{id})$. The process fidelity F_P also determines the average gate fidelity $\bar{F}$ according to the formula $\bar{F}=(dF_P+1)/(d+1)$ (ref. 24), where $\bar{F}$ is defined as the fidelity averaged over all possible input states with equal weight and d is the dimension of the state space (with $d=2$ for a single qubit).